

## Design, calibration and validation of a wheel-rail contact force measurement system in V-Track

Zhang, Pan; Moraal, Jan; Li, Zili

**DOI**

[10.1016/j.measurement.2021.109105](https://doi.org/10.1016/j.measurement.2021.109105)

**Publication date**

2021

**Document Version**

Final published version

**Published in**

Measurement: Journal of the International Measurement Confederation

**Citation (APA)**

Zhang, P., Moraal, J., & Li, Z. (2021). Design, calibration and validation of a wheel-rail contact force measurement system in V-Track. *Measurement: Journal of the International Measurement Confederation*, 175, 1-14. Article 109105. <https://doi.org/10.1016/j.measurement.2021.109105>

**Important note**

To cite this publication, please use the final published version (if applicable). Please check the document version above.

**Copyright**

Other than for strictly personal use, it is not permitted to download, forward or distribute the text or part of it, without the consent of the author(s) and/or copyright holder(s), unless the work is under an open content license such as Creative Commons.

**Takedown policy**

Please contact us and provide details if you believe this document breaches copyrights. We will remove access to the work immediately and investigate your claim.



# Design, calibration and validation of a wheel-rail contact force measurement system in V-Track

Pan Zhang, Jan Moraal, Zili Li\*

*Delft University of Technology, Section of Railway Engineering, Stevinweg 1, 2628 CN, Delft, the Netherlands*

## ARTICLE INFO

### Keywords:

V-Track test rig  
Wheel-rail contact forces  
Dynamometer  
Force measurement and control

## ABSTRACT

An innovative downscale test rig called V-Track has been constructed for wheel-rail contact experiments under impact loading conditions. In this paper, a force measurement system termed a dynamometer was developed in V-Track to measure the wheel-rail contact forces. The dynamometer consists of four 3-component piezoelectric force sensors and was mounted between the wheel assembly and the steel frame of V-Track, enabling it to measure the forces transmitted from the wheel-rail interface to the frame. Static tests were first carried out to calibrate the dynamometer in three directions. Then, several tests were performed in V-Track to examine the reliability and validity of the dynamometer for measuring the wheel-rail contact forces under running conditions. Experimental results show that the dynamometer is capable of reliably and accurately measuring these forces. Utilizing the measurement results from the dynamometer, the control of the wheel-rail contact forces in V-Track has also been achieved.

## 1. Introduction

Railway transport is a major means of transportation worldwide and has become increasingly popular because it is economic, safe and environmentally friendly. In recent years, with increasing train speed and axle loads, more defects have arisen in the wheels and rails, such as rail squats, head checks, corrugation, and wheel polygonization, which considerably increase the maintenance cost. To pinpoint the formation mechanisms of these defects and develop the corresponding countermeasures, an innovative downscale test rig called 'V-Track' has been developed in the laboratory [1] to simulate vehicle-track interactions, as shown in Fig. 1. Compared to other existing test facilities [2–5], V-Track can simulate not only the wheel-rail contact but also the high-frequency dynamics of the vehicle-track system, enabling wheel-rail contact experiments under impact loading in this system. In [1], a potential corrugation after the rail joint in the V-track has been reproduced, which share similar features with an actual corrugation after the rail joint in the Dutch railway network.

Wheel-rail contact force measurement is fundamental to understanding wheel-rail interaction. The forces are responsible for wear, deformation and fatigue of the wheels and rails. Train derailment criteria are based on the amplitudes of the contact forces [6]. For laboratory test facilities, accurate measurement of wheel-rail contact forces

is a prerequisite for force control to simulate different loading conditions from engineering practice, for instance, traction, braking and curve negotiation.

Several measurement approaches for wheel-rail contact forces have been reported in the literature, and they can be classified into two categories, i.e., direct methods and indirect methods. Direct methods typically use an instrumented wheelset equipped with dynamometric sensors to directly measure the forces. For example, Gullers et al. [7] employed strain gauges on a wheel disc to measure vertical wheel-rail contact forces at up to 2 kHz in the field, and four different classes of rail irregularities were identified when evaluating the measured forces. Gomez et al. [8] analyzed two distribution methods of strain gauges based on axle instrumentation and wheel web instrumentation and found that the method based on the axle presented dynamic errors because of the inertia of the wheel mass. Matsumoto et al. [9] proposed a new method in which noncontact gap sensors were mounted on a bogie frame to measure the lateral wheel-rail contact force from the lateral distortion of the wheel. Urda et al. [10] equipped a 1/10 scaled dynamometric wheelset with two technologies: strain gauges and noncontact gap sensors. The results indicated that the technology using strain gauges is a favorable choice for measuring lateral wheel-rail contact forces with high accuracy. Nevertheless, strain gauges are much more expensive than gap sensors because the former require expensive

\* Corresponding author.

E-mail address: [z.li@tudelft.nl](mailto:z.li@tudelft.nl) (Z. Li).

telemetry system(s) to transfer data from the rotating wheelset to the data acquisition system. Another type of direct method utilized strain gauges [11–13] or piezoelectric sensors [14] on the rail web to measure the wheel-rail contact forces. This rail instrumentation method has an advantage over the wheel instrumentation method in that the former does not need an expensive telemetry system for data transmission, but the disadvantage is that the measurement can be performed only at some discrete points of the track.

Indirect methods combine the measurement of vehicle dynamic responses (i.e., acceleration) with a vehicle-track interaction model to derive the wheel-rail contact forces. An example is the work of Xia et al. [15,16], who developed an inverted wagon model to estimate the these forces based only on the measurements of the car body responses. Wei et al. [17] applied the indirect method to derive the wheel-rail contact forces by measuring the accelerations of the bearing box and the relative displacements of the primary suspension. Compared to direct methods, indirect methods are less expensive because the instrumentation on the vehicles is less complicated. One of the limitations is that these methods require a highly accurate vehicle-track computation model to minimize the measurement errors.

The goal of this work is to develop a wheel-rail contact force measurement system on the downscale V-Track. A direct method is preferable because it can directly derive the contact forces and avoid potential errors from the modeling in the indirect method. A continuous measurement is needed when the wheels run on the track, and hence, the measurement system should be developed on the wheel instead of the rail. The instrumented wheel equipped with strain gauges is too expensive and complicated for data transmission with the requirement of a telemetry system. The method using noncontact gap sensors is more cost efficient, but its accuracy is influenced by the position of wheel-rail contact points, and errors are hard to accommodate in practice [9]. In addition to these approaches, Meymand and Ahmadian [18] designed a novel force measurement system using the concept of a dynamometer [19] to measure the wheel-rail contact force. The static calibration of the dynamometer was conducted on a 1/4 scaled roller rig. However, no experimental results were presented to evaluate the validity of the dynamometer for contact force measurements under a real running scenario.

This paper describes the development of a force measurement system in the dynamometer category in a downscale V-Track apparatus for measuring the wheel-rail contact forces in running conditions. Utilizing the measurement results from the dynamometer, the control of these forces was also achieved in V-Track. The paper is organized as follows. Section 2 introduces the structure of V-Track and the design of the dynamometer for the wheel assembly. Section 3 describes the static calibration of the dynamometer. Section 4 measures the wheel-rail contact forces in V-Track under running conditions and examines the reliability and validity of the measurements. Section 5 analyses the

influences of wheel torques and running speeds on the measured contact forces. Section 6 presents the control methods of wheel-rail contact forces in V-Track. The main conclusions are drawn in Section 7.

## 2. Design of the dynamometer in V-Track

### 2.1. Structure of V-Track

V-Track consists of four wheel assemblies running over a ring track system, as shown in Fig. 1. Fig. 2 shows the structure of one of the four wheel assemblies. A wheel (1) with a diameter of 200 mm is fixed on a guiding block (3) through an axle box (2). The position of the wheel along the wheel axle is adjustable. The wheel, axle box, and guiding block move vertically along two parallel guiding shafts (9) under the preloads of two springs (4). The combined stiffness of the two springs is 230 N/mm, which is 1/5 the scale of the primary suspension stiffness of the ICM-type Dutch intercity passenger train. The two springs are loaded at their upper ends by two nuts (6) through load cells (5). By changing the position of the nuts along the threaded part of the guiding shafts, the spring preload can be adjusted between 0 and 7500 N. The wheel angle of attack is also adjustable between  $-2$  degrees and  $+2$  degrees [20]. By adjustment of the angle of attack and the wheel position along the wheel axle, we can simulate various wheel-rail contact conditions of different curvatures in real tracks using the V-Track.

Each of the four wheel assemblies is mounted on an arm of a steel frame (7), shown also in Fig. 1. One motor (the driving motor) is used to drive the steel frame so that wheel assemblies are pulled to move along the ring track. The speed range of the wheel assemblies is between 0 and 40 km/h. Another motor (the braking motor) is connected to the wheels through the braking shafts (8). This motor generates a torque in the opposite direction of the driving torque so that a braking force arises at the wheel-rail contact. The braking torque applied by the braking motor can be measured by torque sensors in each of the four braking shafts and can be controlled. Thus, each wheel works like a wheel in an unpowered vehicle: it is pulled by the vehicle (the steel frame on V-Track) and rolls almost freely forward. It should roll almost freely because (ideally) there should be no frictional tangential contact force at the wheel-rail interface. In reality, resistance in the load path of the wheel, e.g., in bearings, causes a (usually small) tangential contact force. A large tangential contact force has to be intentionally applied by, e.g., a braking system. In V-Track, this is the braking torque from the braking motor applied via the braking shaft. A more detailed description can be found in [1].

The ring track, which has a radius of 2 m, consists of three pieces of rails connected by three fishplate rail joints, as shown in Fig. 3a. The choice of the V-Track's radius (2 m) was mainly driven by its bulkiness. This radius is geometrically not representative of the typical curvatures encountered in real tracks. Yet the physical vehicle-track lateral interaction, especially wheel-rail lateral interaction, can be simulated in V-

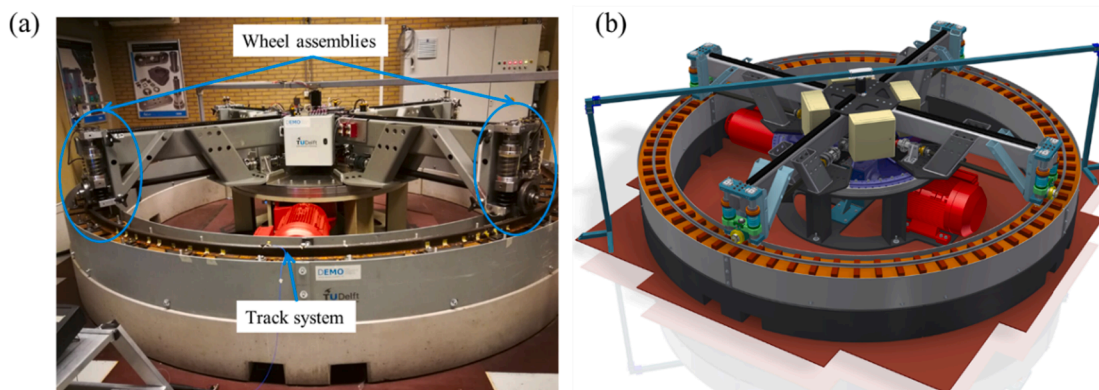


Fig. 1. Downscale V-Track for wheel-rail contact experiments. (a) V-Track developed in the laboratory; (b) schematic CAD drawing of V-Track.

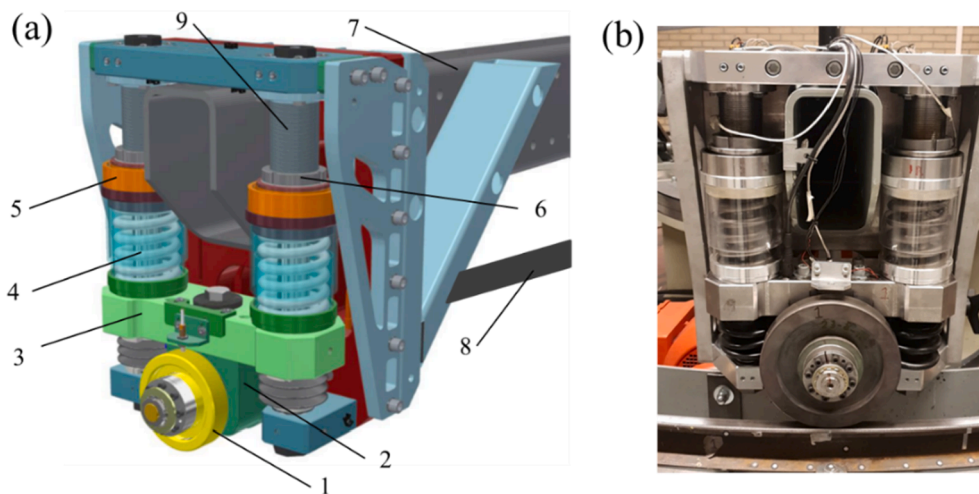


Fig. 2. Structure of one wheel assembly of V-Track. (a) Schematic drawing in CAD: 1) wheel, 2) axle box, 3) guiding block, 4) suspension springs, 5) load cells, 6) preload nut, 7) steel frame, 8) braking shaft, and 9) guiding shaft; (b) single wheel assembly in V-Track.

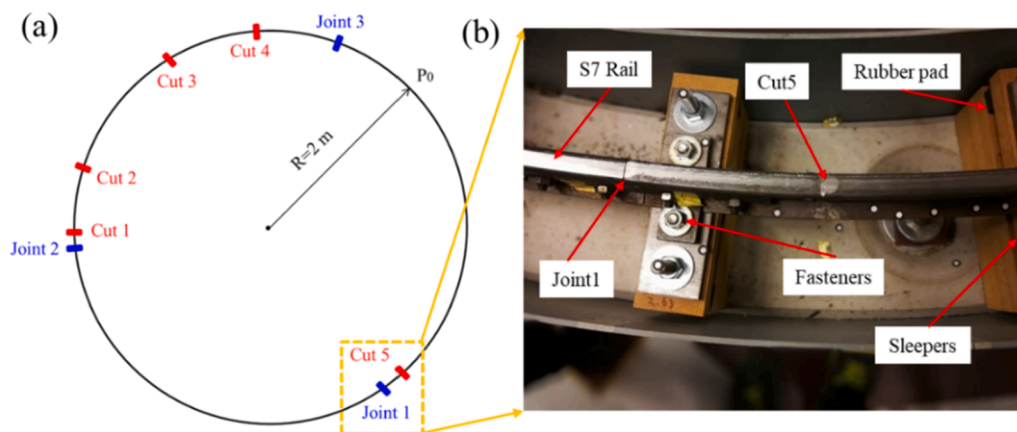


Fig. 3. The track structure of V-Track. (a) Cuts and joints on the ring track; (b) main track components.

Track. For instance, V-Track cannot generate the centrifugal force of trains experienced in curved track, but the effects of such a lateral force on wheel-rail contact and vehicle-track interaction can be generated and investigated in V-Track by properly setting (1) the angle of attack, (2) the rail inclination and (3) the wheel conicity. The ring rail, which has a

standard S7 profile is supported on steel plates. The standard S7 rail is defined in German norm DIN 5901. It has a mass of 6.75 kg per meter and is thus called “S7”. The rail and plates are fixed on wooden sleepers by fasteners, as shown in Fig. 3b. The sleeper spacing is 0.4 m. Different numbers of steel pads are placed between the rail and the steel plates to

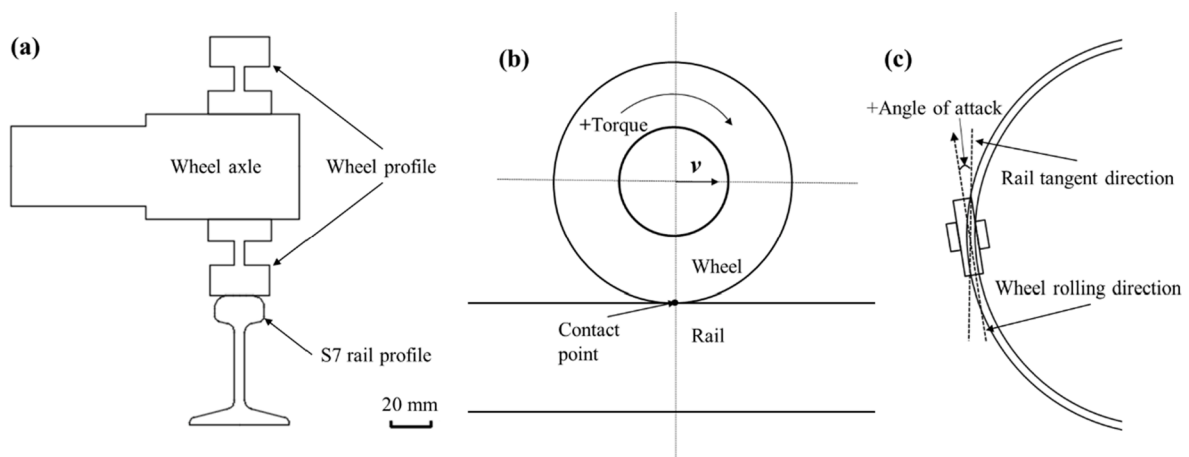


Fig. 4. The schematic drawing of the wheel-rail contact system in V-Track. (a) Cross-section of wheel-rail contact; (b) side view of the wheel-rail system; (c) top view of the wheel-rail system with a positive angle of attack.

adjust the track vertical irregularity. Underneath the sleepers are rubber pads, which are used to simulate the elasticity and damping of ballast layers in the real-life track. Five artificial cuts with different widths and depths were made on the rail surface to excite high-frequency wheel-rail forces, which may induce rail squats or short pitch corrugation. The positions of the five cuts and three rail joints are shown in Fig. 3a. The position  $P_0$  in Fig. 3a is the origin position to start data recording.

Fig. 4 presents the schematic drawing of the wheel-rail contact system in V-Track. The cross-section of the wheel-rail contact system is shown in Fig. 4a. Fig. 4b shows the side view of the wheel-rail system. The upper arrow indicates the positive direction of braking torque, which generates a traction force at the wheel-rail interface. On the contrary, a negative braking torque will generate a braking force at the wheel-rail interface. Fig. 4c shows the top view of the wheel-rail contact system with a positive angle of attack.

The designed maximum vertical load is 7500 N per wheel, which is equivalent to a static axle load of approximately 380 kN, considering a scale factor of 1/5. The maximum allowed longitudinal and lateral forces are both 3750 N with a friction coefficient of 0.5.

### 2.2. Design of the dynamometer

The dynamometer consists mainly of four 3-component piezoelectric force sensors (Kistler, type 9067C) mounted between 2 steel plates, as shown in Fig. 5a. A set of high-strength preloading bolts are used to

connect the two plates and provide the force sensors with the necessary preload. The shear forces are transmitted through static friction from one plate to the other. Each force sensor contains three pairs of quartz plates to measure the three orthogonal components of the applied static and dynamic forces. The technical data of the Kistler force sensor type 9067C are shown in Table 1 [21].

After assembly (see Fig. 5a), the dynamometer was installed in V-Track, as shown in Fig. 5b–e. The directions of the dynamometer are aligned with the kinematic coordinate system of the wheel assembly, with the axes  $x$ ,  $y$ , and  $z$  oriented in the longitudinal (rolling), lateral and

**Table 1**

The technical data of the Kistler force sensor type 9067C.

Range	$F_{x,z}$ $F_z$	kN	-30...-30
	$F_y$ <td>kN <td>-60...-60</td> </td>	kN <td>-60...-60</td>	-60...-60
Calibration range	$F_{x,z}$ $F_z$ <td>kN <td>0...30</td> </td>	kN <td>0...30</td>	0...30
	$F_y$ <td>kN <td>0...30</td> </td>	kN <td>0...30</td>	0...30
Sensitivity	$F_{x,z}$ $F_z$ <td>pC/N <td><math>\approx -8.1</math></td> </td>	pC/N <td><math>\approx -8.1</math></td>	$\approx -8.1$
	$F_y$ <td>pC/N <td><math>\approx -3.9</math></td> </td>	pC/N <td><math>\approx -3.9</math></td>	$\approx -3.9$
Linearity, each axis		%FSO <td><math>\leq \pm 0.25</math></td>	$\leq \pm 0.25$
Hysteresis, each axis		%FSO <td><math>\leq 0.25</math></td>	$\leq 0.25$
Crosstalk	$F_y \rightarrow F_{x,z}$ $F_z$	%	$\leq \pm 0.5$
	$F_x \leftrightarrow F_z$	%	$\leq \pm 2$
	$F_{x,z}$ $F_z \rightarrow F_y$	%	$\leq \pm 3$
Operating temperature range		$^{\circ}\text{C}$	-40...120

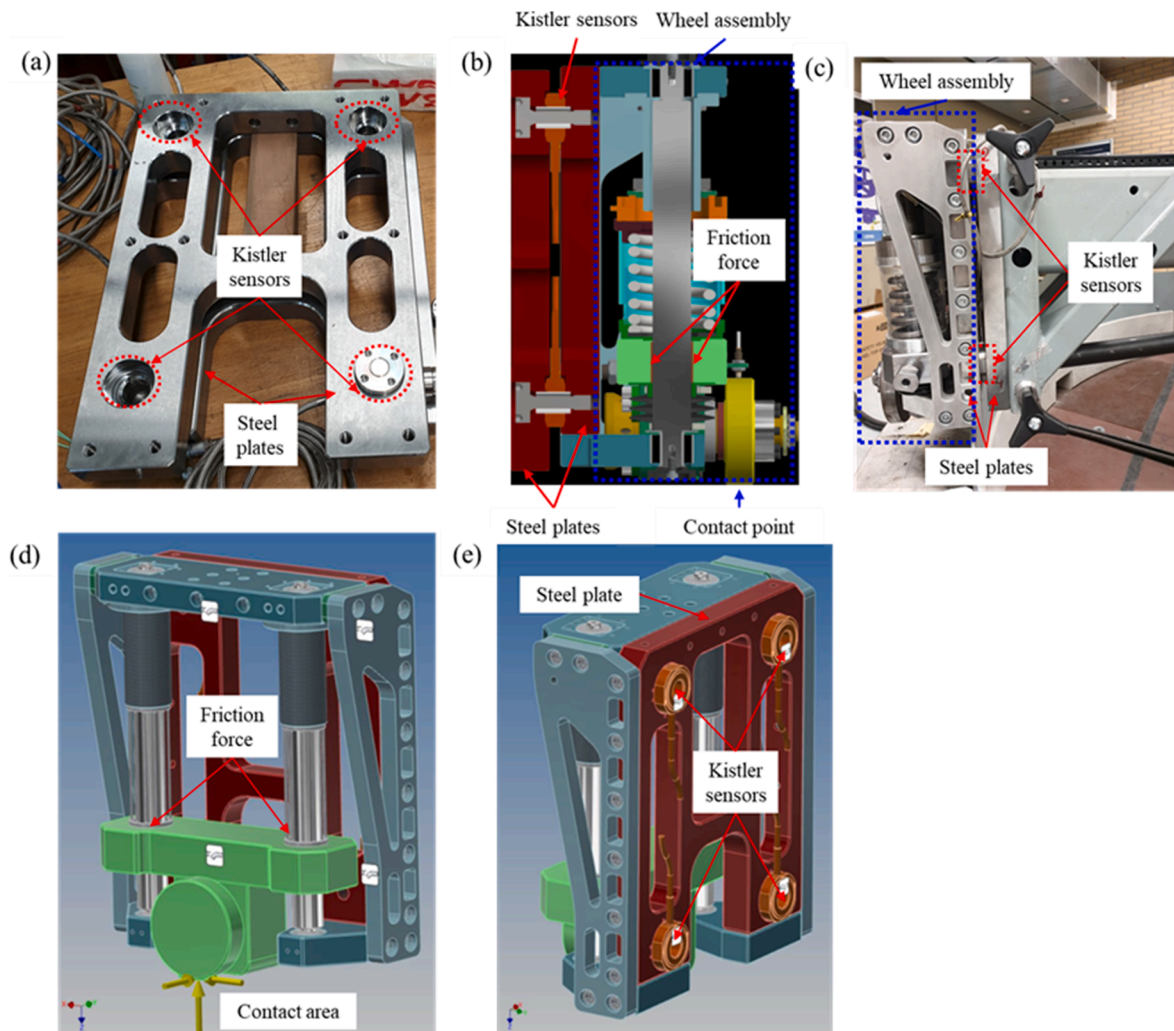


**Fig. 5.** The designed dynamometer in V-Track. (a) Kistler force sensors between two steel plates; (b) the cross-section of the dynamometer in the V-Track schematic drawing; (c) the dynamometer in V-Track; (d) Contact forces acting in the contact area; (e) the position of the dynamometer in V-Track.

vertical directions, respectively. The dynamometer forces in the three directions are calculated by the summation of the output from the four force sensors as follows:

$$F_x = F_{1x} + F_{2x} + F_{3x} + F_{4x}; \quad (1)$$

$$F_y = F_{1y} + F_{2y} + F_{3y} + F_{4y}; \quad (2)$$

$$F_z = F_{1z} + F_{2z} + F_{3z} + F_{4z}; \quad (3)$$

where  $F_x$ ,  $F_y$ , and  $F_z$  are the dynamometer forces in the longitudinal, lateral and vertical directions and  $F_{ix}$ ,  $F_{iy}$ , and  $F_{iz}$  ( $i = 1, 2, 3, 4$ ) are the  $i^{\text{th}}$  sensor forces in the longitudinal, lateral and vertical directions, respectively.

According to the equilibrium of the wheel assembly, the longitudinal wheel-rail contact force can be calculated as follows:

$$F_{conx} = F_x + \sum m_j a_{jx} \quad (4)$$

where  $F_{conx}$  is the wheel-rail contact force in the longitudinal direction,  $F_x$  is the measured dynamometer force in the longitudinal direction,  $m_j$  is the mass of the  $j^{\text{th}}$  component of the wheel assembly which is indicated by blue dashed lines in Fig. 5b and c, and  $\sum m_j a_{jx}$  is the total inertia force of the wheel assembly in the longitudinal direction,  $j = 1, 2, \dots$ , denoting components like the wheel, axle box, guiding block, guiding axis. Eq. (4) indicates that the wheel-rail contact forces comprise two components: one is the inertia force of the wheel assembly, and the other is the force transmitted to the frame through the dynamometer. If we reduce the loading condition to a (quasi)static state in which the accelerations of the system are zero, the dynamometer forces can be regarded as equal to the wheel-rail contact forces, as follows:

$$F_{conx} = F_x \quad (5)$$

In the measurements described in the following sections, the inertia force of the wheel assembly is not considered. This arrangement applies to most situations except at the cuts and joints where large impact vibrations occur so that the inertia forces are large. Further research is needed on the compensation of the wheel inertia forces to more accurately measure the dynamic contact forces.

### 3. Static calibration

Before running tests on V-Track, a static calibration of the dynamometer is needed to check whether the force sensors can work

satisfactorily and whether the sensitivity parameters given by the manufacturer in Table 1 are precise. In this section, the static calibration setups in three single directions ( $x, y, z$ ) are described, as shown in Fig. 6. In addition, the accuracies and crosstalk errors of the dynamometer are evaluated. The static calibration with loads in arbitrary directions were not conducted to avoid errors from the force decomposition.

#### 3.1. Setup for static calibration

The setup for the vertical calibration is shown in Fig. 6a. A crane was used to apply a vertical force to the wheel axle by a sling. A load sensor was mounted between the crane and the sling to record the crane force. The sling was configured to be as vertical as possible to avoid force components in the other two directions. The crane force was increased step by step up to 9000 N, larger than the designed maximum vertical preload (7500 N). The data of the dynamometer were recorded with a sampling frequency of 1 Hz.

The longitudinal and lateral calibration cannot be conducted directly on V-Track as the vertical calibration is because the crane can apply a vertical force only. Therefore, the dynamometer together with the wheel assembly was detached from V-Track. For the longitudinal calibration, the dynamometer and wheel assembly were rotated 90 degrees and mounted on a vertical rigid I beam to ensure that the longitudinal direction became vertical, as shown in Fig. 6b. A crane and sling were used to apply a nominally longitudinal wheel-rail contact force. The crane force was increased step by step up to 4000 N, larger than the designed maximum longitudinal force (3750 N).

For the lateral calibration, the dynamometer and wheel assembly were rotated 90 degrees and mounted horizontally on a rigid frame to ensure that the lateral direction of the system became vertical, as shown in Fig. 6c. A crane and sling were used to simulate lateral force applied to the system. The crane force was increased step by step up to 8000 N.

Before the calibration of the dynamometer, the accuracy of the crane load sensor was first examined to ensure a good reference. Weight blocks in approximately 13.2 kg intervals were applied to the crane up to 532.2 kg. The largest error of the crane load sensor compared to the block weight was found to be less than 0.6%, which is acceptable for calibration.

#### 3.2. Results for static calibration

Three repeated measurements were performed in each direction, and similar values were obtained, which verified the consistency of the

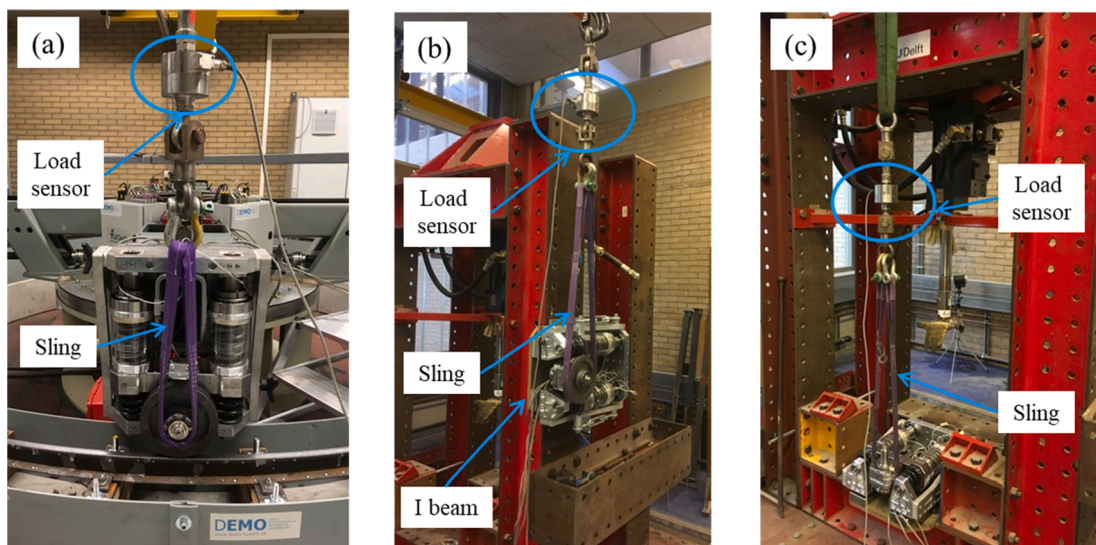


Fig. 6. Setups for static calibration of the dynamometer. (a) Vertical setup; (b) longitudinal setup; (c) lateral setup.

measurement. Fig. 7a–c show one of the measured results in the vertical, longitudinal and lateral directions, respectively.

In the longitudinal direction, the dynamometer measured the crane force with a high accuracy of 99.05%. The crosstalk errors in the vertical and lateral directions were 0.28% and 1.79%, respectively. The adjusted R-Squares of these three linear fittings in Fig. 7a are 99.99%, 99.93%, 98.40%. In the vertical direction, the accuracy of the dynamometer was 99.04%. The crosstalk errors in the longitudinal and lateral directions were 1.04% and 1.03%, respectively. The adjusted R-Squares of these three linear fittings in Fig. 7b are 99.48%, 99.99%, 99.94%. In the lateral direction, the accuracy of the dynamometer was 95.62%, slightly lower than those in the other two directions. The crosstalk errors in the longitudinal and vertical directions were 0.30% and 0.87%, respectively. The adjusted R-Squares of these three linear fittings in Fig. 7c are 94.60%, 99.53%, 99.99%.

Overall, a high accuracy of the dynamometer was achieved in measuring the static forces in the three directions, indicating that the force sensors worked properly and that the given sensitivity parameters in Table 1 were precise. Compared to the longitudinal and vertical directions, the accuracy in the lateral direction was lower (95.62%), and the crosstalk errors from the other two directions were higher (1.79%, 1.04%). The reason may be that the lateral force is measured based on the compression pressure of the quartz plates and is less sensitive than the shearing in the longitudinal and lateral directions, as shown in Table 1. Nevertheless, the maximum crosstalk error of 1.79% was considered acceptable in the current work. Future research will be performed to further reduce it.

#### 4. Validation of running tests

After the static calibration, the wheel assembly and dynamometer were mounted to V-Track. In this section, we examined the repeatability and validity of the dynamometer to measure the wheel-rail contact forces under running conditions.

##### 4.1. The repeatability of measurements in running conditions

The running speed of the wheel assemblies on the ring track was 4 km/h. The wheel preload was 4500 N. No braking torque was applied on the wheel by the braking motor. The angle of attack was not measured. The wheel-rail contact forces in the three directions were measured by the dynamometer with a sampling frequency of 16.67 kHz. In each direction, the data were recorded for three rounds of wheel rolling along the ring to examine the repeatability of the measurements, as shown in Fig. 8. The starting (0 m) and ending positions (12.56 m) in Fig. 8 correspond to the same position  $P_0$  in Fig. 3a.

Fig. 8a–c show very good repeatability of the measurements in the three directions, indicating that the dynamometer can reliably measure the wheel-rail contact forces under running conditions.

Fig. 8a shows that the measured longitudinal force along the track is not constant but changes significantly at different positions. It first increases from 407 N at  $P_0$  to a maximum value of 933 N at 5.44 m and then gradually decreases. Considering that no braking torque was applied, the longitudinal force is unexpectedly large. The reasons are discussed in Section 4.3.1.

The measured vertical force in Fig. 8b shows strong fluctuation between approximately 4 kN and 5 kN, which is expected to arise from the vertical track irregularity. When the wheel runs over the track, the

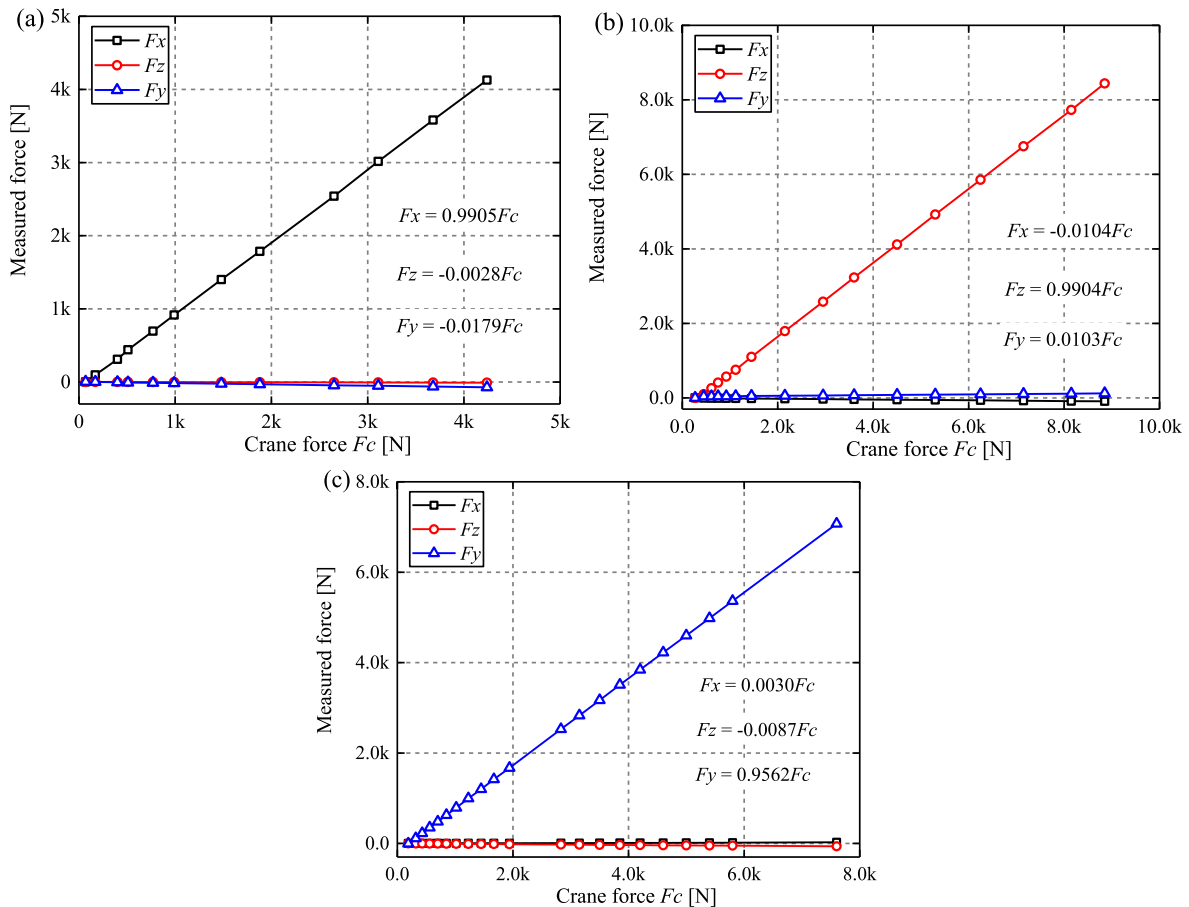
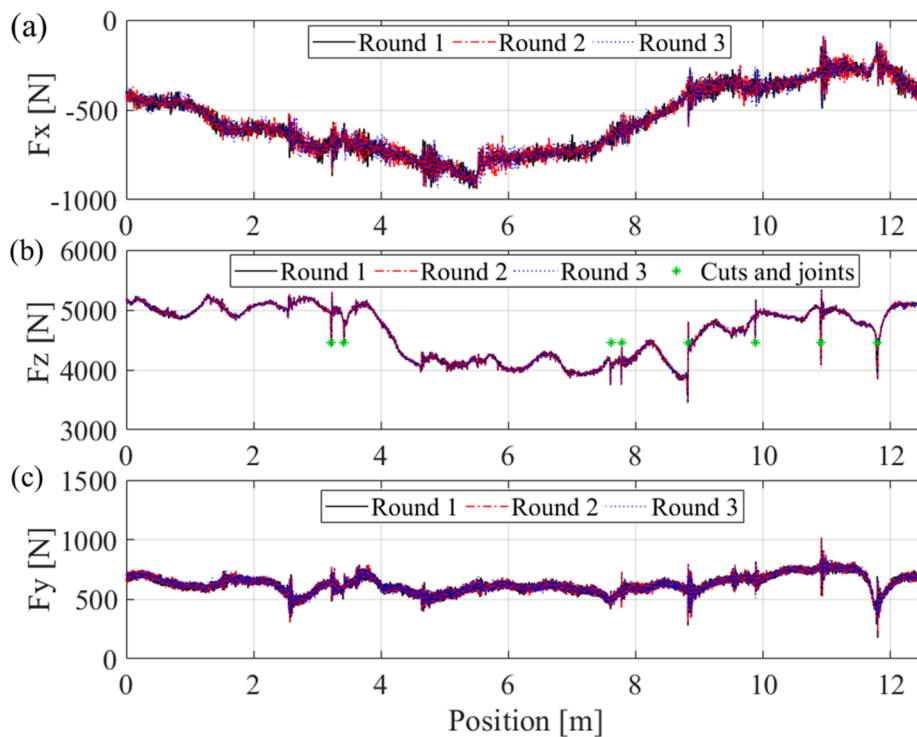


Fig. 7. Results of static calibration in the (a) longitudinal direction, (b) vertical direction, and (c) lateral direction.  $F_c$  denotes the crane force.



**Fig. 8.** Measured wheel-rail contact forces under running conditions in three directions. (a) Longitudinal force, (b) vertical force, (c) lateral force. The green stars in Fig. 8b indicate the positions of cuts and rail joints. The running speed was 4 km/h, and the wheel preload was 4500 N. (For interpretation of the references to colour in this figure legend, the reader is referred to the web version of this article.)

length of the suspension springs varies because the upper ends of the springs are fixed on the frame while the lower ends go up and down, following the vertical track irregularity, leading to the fluctuation of the vertical force. Eight sharp peaks are observed in this figure, and their positions correspond to those of the three rail joints and five artificial

cuts, indicated by the green stars in Fig. 8b. This demonstrates that the dynamometer can capture the dynamic features of the wheel-rail impact vibrations, although it may not be currently capable of quantitatively measuring the impact forces without considering the inertia forces of the wheel assembly.

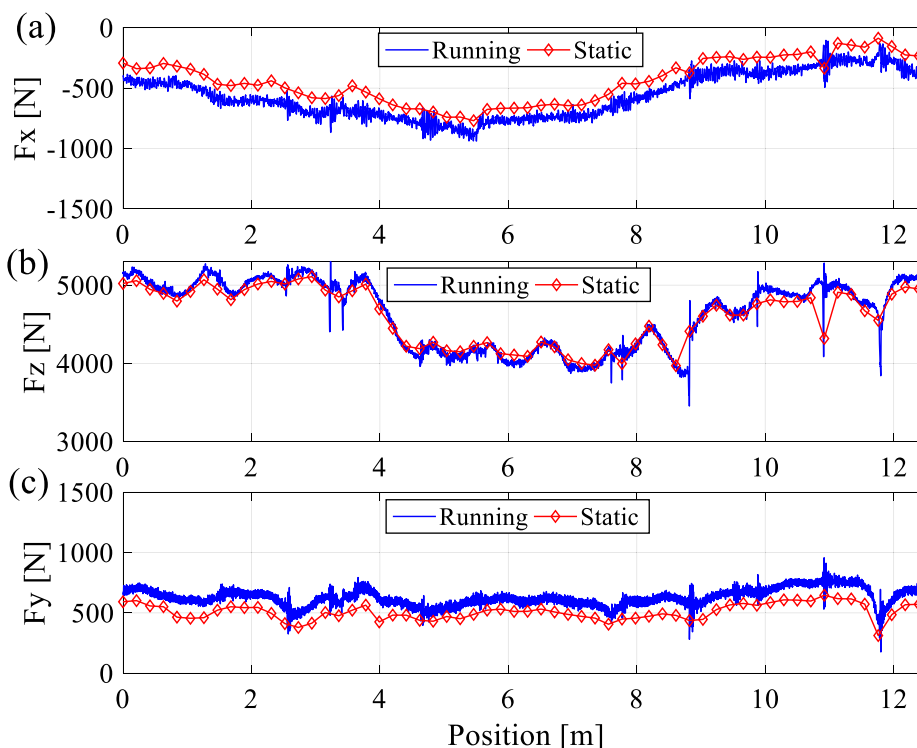


**Fig. 9.** Measured wheel-rail contact forces by the dynamometer under static and running conditions. (a) Longitudinal force, (b) vertical force and (c) lateral force.

Compared to the measured longitudinal and vertical forces, the overall lateral force response is relatively flat, varying in the range of approximately 500 N-750 N, as shown in Fig. 8c. This indicates that an angle of attack exists between the wheel and the rail, which must be constant along the track.

#### 4.2. Validation by a static measurement

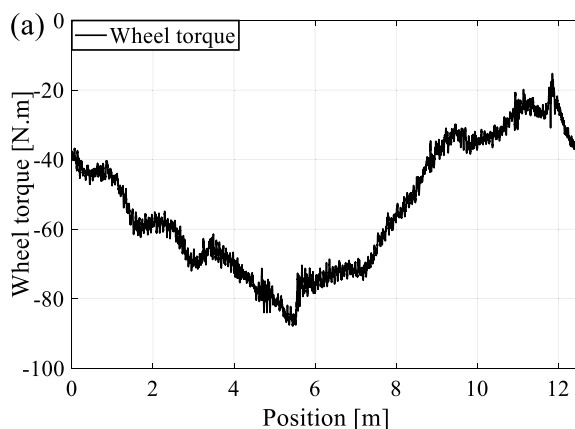
The static force measurement calibration of the dynamometer is described in Section 3. Therefore, in this section, we describe using the dynamometer to measure the static wheel-rail contact forces in V-Track and compare them with those in the running condition. The wheel preloads, braking torques, and angle of attack in this static measurement are the same as in Section 4.1. The only difference is that the wheel assemblies are manually pushed forward along the ring track in the static tests and stopped every 0.2 m instead of continuously running as driven by the driving motor in the running tests. The stopping positions are either above the track supports ('on-support') or at the middle of two supports ('at midspan') to consider the influences of different track support stiffnesses on the contact forces. The measured forces by the dynamometer are recorded when the wheel assemblies stand still, corresponding to the static wheel-rail contact forces.

The measured static wheel-rail contact forces are compared with those in the running test in Fig. 9. Overall, good agreement between these two cases is achieved in the three directions, indicating that the dynamometer can accurately measure the wheel-rail contact forces under running conditions. The results also reveal that the loading of V-Track is approximately quasistatic under these conditions, indicating that our arrangement—which does not consider the inertia forces of the wheel assembly—is appropriate in these cases. At the rail joints and cuts, the static measurement does not capture the impact forces, which can be observed from the running tests.

Fig. 9 shows that the longitudinal and lateral forces are reduced by approximately 110 N in the static measurement. This amplitude difference is probably caused by frictional interlocking in the load chains in V-Track. Additionally, in the lateral direction, the centrifugal force of the wheel assembly is another source of this reduction, which is approximately 55 N considering the wheel assembly mass of approximately 90 kg.

#### 4.3. Validation by wheel torque and spring load measurement

In addition to the dynamometer, the torque sensors in the braking shafts and load cells ((5) in Fig. 2a) along the guiding shafts can be used to estimate the longitudinal and vertical wheel-rail contact forces. In this section, we compare the measurement results from the dynamometer with those from the torque sensors and the load cells.



#### 4.3.1. Validation of longitudinal force by wheel torque measurement

In Section 4.1, it was found that the measured longitudinal wheel-rail contact force was unexpectedly large, although no braking torque was applied on the wheel by the braking motor. In this section, the measured torque from the torque sensor is as depicted in Fig. 10a. The torque is not zero but changes considerably along the track with a maximum value of approximately 88 N.m. The negative torque generates a braking force at the wheel-rail interface, which can be calculated as follows:

$$F_{xc} = M_w / r_w \tag{6}$$

where  $F_{xc}$  is the calculated longitudinal force,  $M_w$  is the measured torque from the torque sensor, and  $r_w$  is the radius of the wheel, which is 0.1 m.

Fig. 10b compares the longitudinal force calculated from the measured torque and the longitudinal force measured by the dynamometer. The good agreement confirms that the dynamometer can accurately measure the longitudinal wheel-rail contact force. The negative torque is expected to arise from the resistance in the load chain of V-Track, including the gearbox and the braking motor. This resistant torque can be compensated by applying a positive torque to the wheel by the braking motor.

#### 4.3.2. Validation of vertical force by spring load measurement

The vertical spring loads can be measured by the load cells ((5) in Fig. 2a). Fig. 11 compares the vertical wheel-rail contact force measured from the dynamometer and the spring loads from the load cells. Both

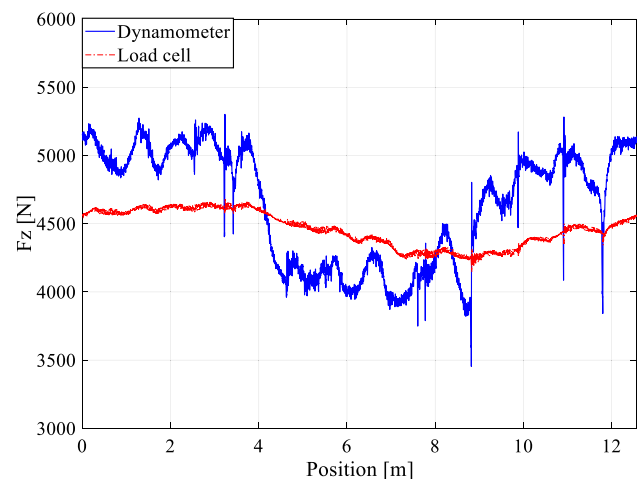


Fig. 11. Comparison of vertical contact force from the dynamometer and the spring load from the load cells.

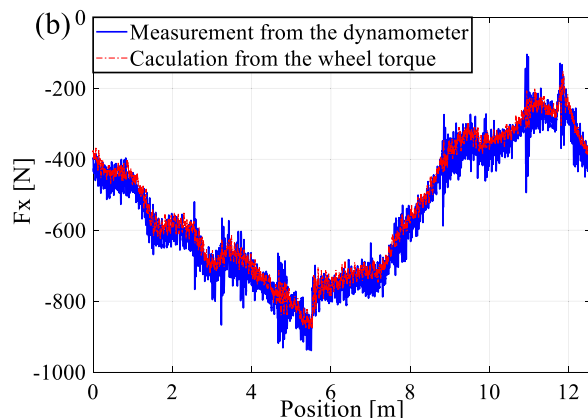


Fig. 10. Validation of the measured longitudinal wheel-rail contact force by wheel torque measurement: (a) measured wheel torque; (b) comparison of the calculation from wheel torque and the measurement from the dynamometer.

measurements fluctuate by approximately 4500 N and have a similar tendency: first, they are relatively flat between 0 m and 3.8 m, then go down from 3.8 m to 8.8 m, and gradually rise after 8.8 m. However, the dynamometer results show much stronger fluctuation.

To understand the difference in these two cases, the static spring deformation was measured along the track by a digital dial indicator, as shown in Fig. 12a. The dial indicator was mounted firmly to the frame by an adjustable magnetic base. The needle of the dial indicator vertically contacted the guiding block. Therefore, the dial indicator measured the relative displacement between the guiding block and the frame, which was also the spring deformation. We manually pushed the wheel assemblies running along the track and stopped every 0.2 m and recorded the readout of the dial indicator when stopping. This process was similar to the static measurement in Section 4.1. The resolution of the dial indicator was 0.01 mm.

The measured static spring deformation along the track is shown in Fig. 12b. The spring deformation in the running tests can be estimated as follows:

$$d_s = F_l/k_s \quad (7)$$

where  $d_s$  is the calculated spring deformation in the running condition,  $F_l$  is the measured spring load from the load cells, and  $k_s$  is the stiffness of the springs. The calculated spring deformation under running conditions is compared with the deformation measured under static conditions in Fig. 12b. The good agreement between them shows that the load measured from the load cells is quasistatic under the running conditions, except for the impacts at the rail joints and cuts.

Fig. 9 shows that the vertical force measured by the dynamometer is also quasistatic under running conditions. Therefore, the difference between the dynamometer and the load cells should also be caused by a (quasi)static force. To identify the source of this force, static tests were performed at three positions on the track: 0 m, 1.6 m and 4 m. In these tests, the wheel-rail contact was first loaded by tightening and then unloaded by loosening the preload nuts step by step. The vertical force measured by the dynamometer and the spring load measured by the load cells are shown in Fig. 13. The hysteretic relationships between them in these three positions are similar and illustrate that there is a friction force in the load path between the wheel-rail interface and the dynamometer.

The structure of the wheel assembly in Fig. 2 indicates that such friction force can exist only between the guiding block and the guiding shafts. The wheel plane is out of the plane formed by the two guiding shafts, causing normal contact forces between the guiding block and guiding shafts. The friction force occurs when the guiding block slides

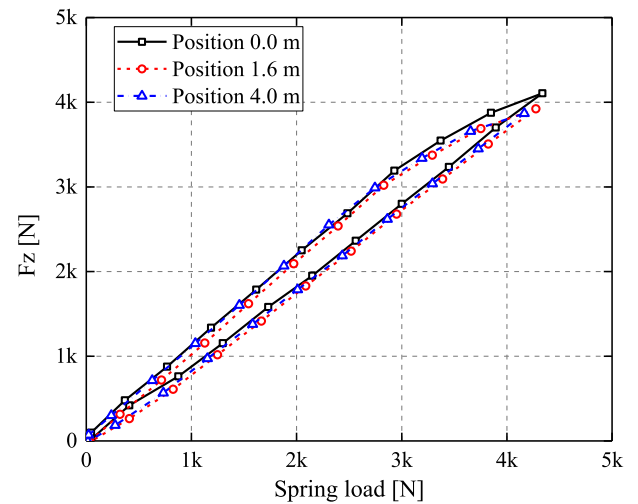


Fig. 13. The relationship between the spring load from the load cells and the vertical contact force from the dynamometer.

along the guiding shafts.

Therefore, the difference between the vertical contact force measured by the dynamometer and the spring loads by the load cells can be explained as follows: the vertical wheel-rail contact force transmits to the dynamometer through two load paths. One is through the suspension springs and load cells, and the other is via the friction between the guiding block and guiding shafts. The contact between the guiding block and guiding shafts has a higher stiffness than the suspension springs, and the high-frequency dynamic force can be transferred to the dynamometer without the buffering of the springs, enabling the dynamometer to capture the dynamic features of the wheel-rail impact vibrations.

## 5. Influencing factors

### 5.1. The influence of braking torques on contact forces

In the experiments described in Section 4, no braking torque was applied on the wheels by the braking motor in the running tests. This section describes how nine braking torques were used to analyze their influence on the measured wheel-rail contact forces. The torques were 0, -50, -100, -150, -200, -250, -275, -285, and -300 N.m. The braking torque was applied through one gearbox, which distributes the

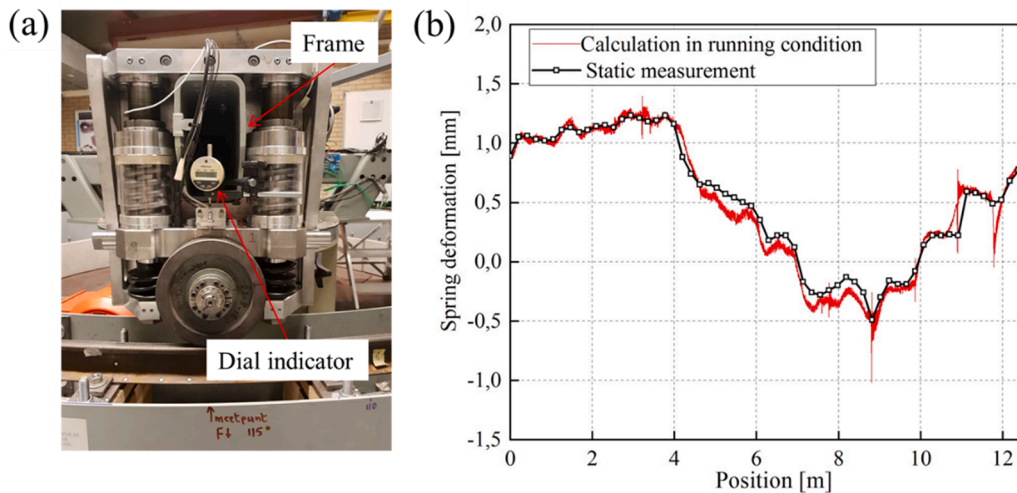


Fig. 12. Comparison of the spring deformation along the track under static and running conditions. (a) Setup for static measurement; (b) comparison of the spring deformation under static and running conditions.

torque onto the four wheels. When the braking torque was increased to slightly larger than  $-300$  N.m, wheel skidding occurred with sparks at the wheel-rail interface, which indicated that the tangential creep force reached the saturation value. In this condition, the coefficient of friction  $f$  between the wheel and the rail is determined with the Coulomb friction law (8).

$$f \leq \sqrt{F_x^2 + F_y^2} / F_z \quad (8)$$

Fig. 14 shows the measured wheel-rail contact forces under different torques. The longitudinal force increases with increasing braking torque. The increment between 4 m and 8 m is smaller than at the other positions because (1) the original longitudinal force without braking torque is larger in this position (see Fig. 9(a)) and is thus closer to the saturation value and (2) the saturated longitudinal force between 4 m and 8 m (with  $-300$  N.m) is also smaller than other positions because the corresponding vertical force in 4–8 m is small and the saturated longitudinal force cannot exceed the limit of vertical force times friction coefficient, according to the Coulomb friction law (8). The vertical contact force remains almost the same under the different braking torques, as expected. The lateral contact force shows a decreasing trend with increasing braking torque, as at each point in the wheel-rail contact patch, the longitudinal component of the tangential contact stress increases, whereas the maximum tangential stress is bounded by the Coulomb friction law (8). The friction coefficient is approximately 0.25, calculated with (8) under a torque of  $-300$  N.m.

To better understand the experimental results, the theoretical creep force-creepage curves were calculated using Kalker's CONTACT [22]. The longitudinal and lateral creepage were calculated as follows,

$$v_x = (|v| - |c|) / v \quad (9)$$

$$v_y = \alpha \quad (10)$$

Where  $v_x$  and  $v_y$  are the longitudinal and lateral creepage,  $v$  is actual forward velocity,  $c$  is pure rolling forward velocity,  $v$  is forward velocity,  $\alpha$  is angle of attack. The longitudinal and lateral forces were solved based on Kalker's exact three dimensional rolling contact theory where

linear elastic half-space assumption was applied. To consider nonlinear material properties (i.e. elasto-plastic) and wheel-rail dynamic effects, the explicit FEM has been proven to be suitable [23,24], which will be used in future work. The calculated creep force-creepage curves were shown in Fig. 14a. In this calculation, the normal load is 5250 N, which is the vertical contact force at the track position of 0.5 m. The friction coefficient is 0.25. The angle of attack is assumed to be constant at this position with the different braking torques, and its value is taken as 0.8 mrad in the calculation, which is estimated by CONTACT based on the measured contact forces. The longitudinal creepage is varied from 0 to 1% to simulate the different braking torque conditions in the tests.

Fig. 15a shows that the longitudinal creep force increases with increasing longitudinal creepage before reaching the saturation point, while the lateral creep force shows a decreasing trend. This explains the measurement results in Fig. 14 that the longitudinal contact force increases while the lateral contact force decreases when the braking torque increases. According to the curves in Fig. 15a, the relationship between the longitudinal and lateral forces can also be obtained, as shown in Fig. 15b. The lateral creep force first gradually decreases with increasing longitudinal creep force and then drops dramatically when the total tangential force reaches the saturation value. The measured longitudinal and lateral contact forces at position 0.5 m and 2.15 m under the nine braking torque conditions are compared with the calculated curve in Fig. 15b. The agreement between the calculation and measurement confirms the validity of the dynamometer for contact force measurement in the longitudinal and lateral directions.

### 5.2. The influence of running speeds

In the experiments described in Section 4, the running speed of the wheel assemblies on the ring track was 4 km/h. In the work described in this section, the running speed was increased to 10, 15, and 20 km/h; the measured forces from the dynamometer are shown in Fig. 16.

Fig. 16a and 16b show that the longitudinal and vertical contact forces change little with increasing speed, which confirms that the loading condition of V-Track is approximately quasistatic. The measured

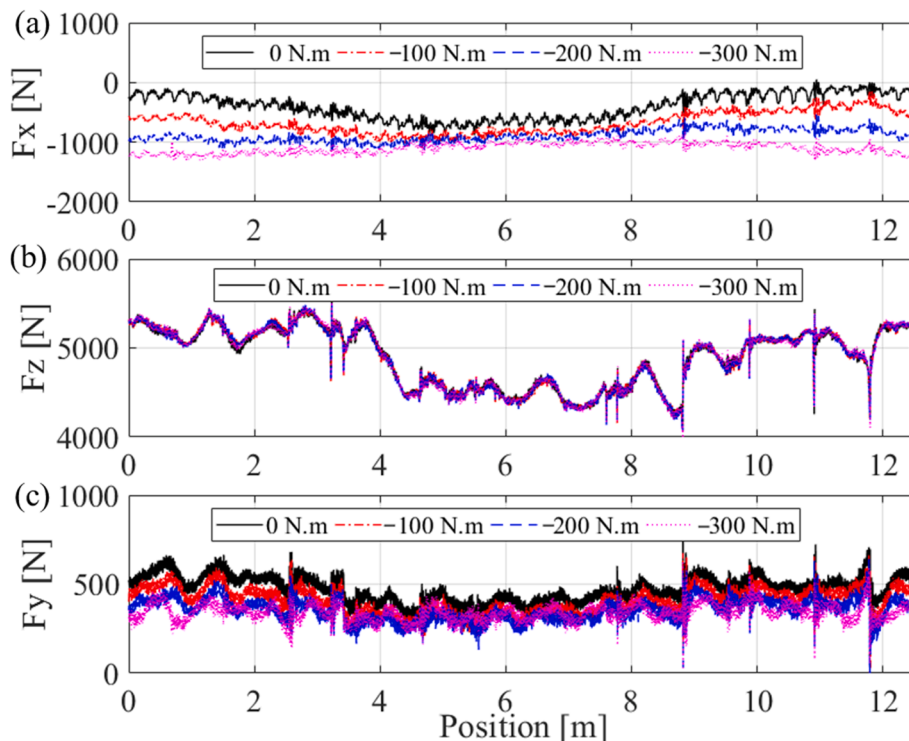


Fig. 14. Measured wheel-rail contact forces under different braking torques from the braking motor. (a) Longitudinal force, (b) vertical force and (c) lateral force.

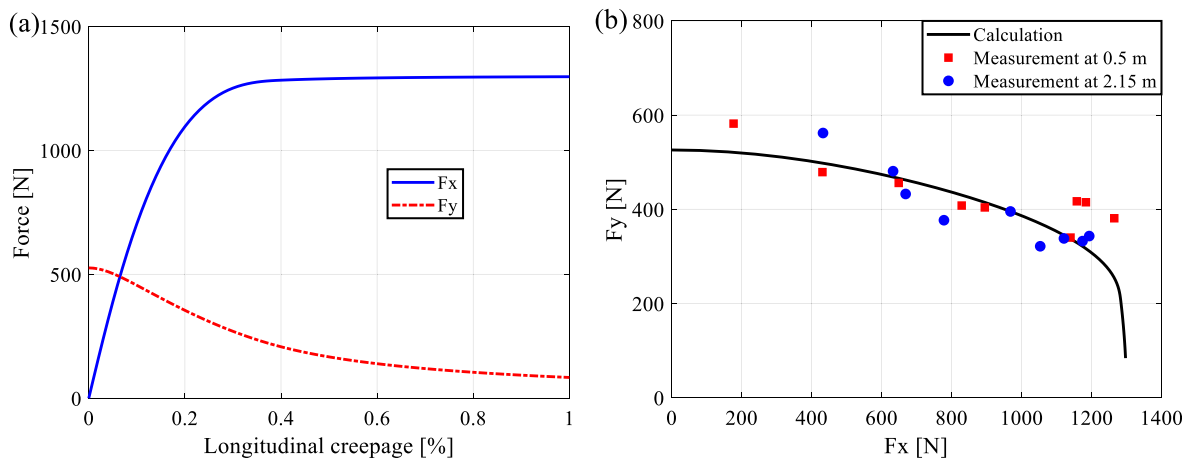


Fig. 15. The relationship between the longitudinal and lateral forces. (a) Calculated creep force/creepage curves; (b) the calculated and measured relationship between the longitudinal and lateral creep forces.

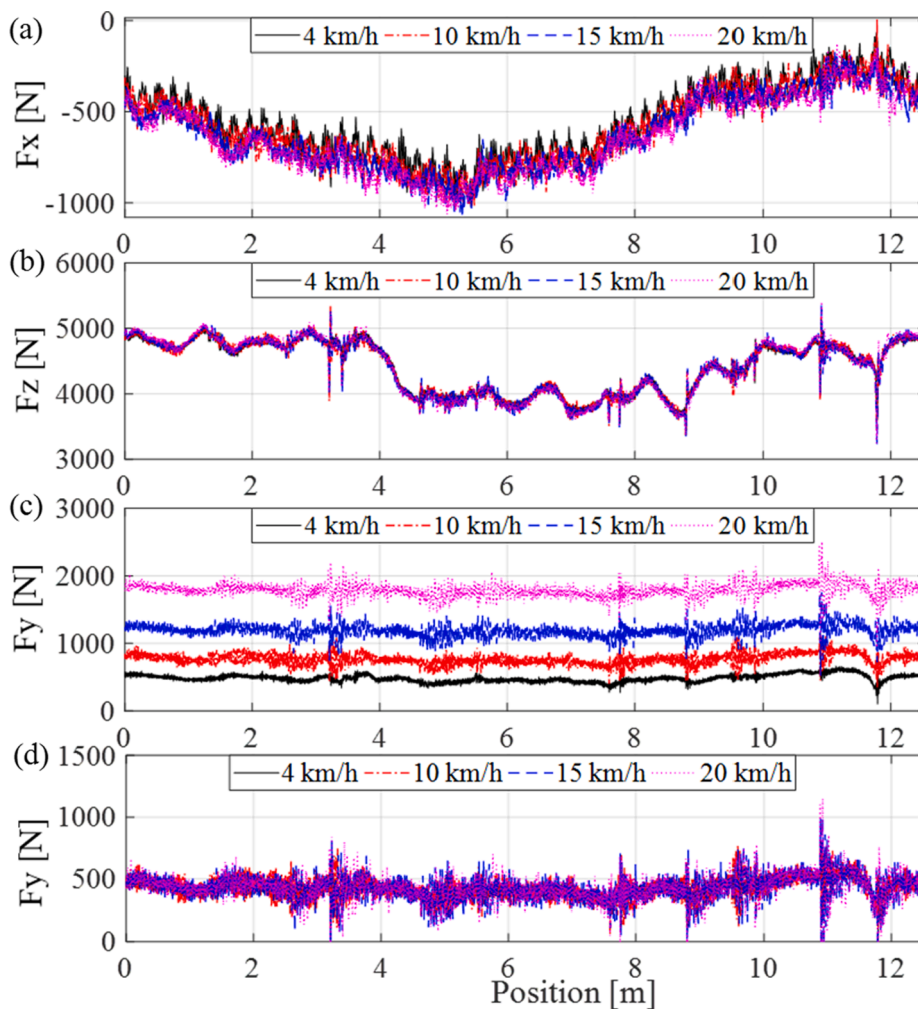


Fig. 16. Measured wheel-rail contact forces with different running speeds: (a) longitudinal force, (b) vertical force and (c) lateral force before compensation, (d) lateral force after compensation.

lateral force significantly increases with increasing speed, and the increment is almost uniform along the whole track, as shown in Fig. 16c. These increments are caused by the increasing centrifugal force of the wheel assembly at higher running speeds. According to Equation (4), the dynamometer needs to compensate for the centrifugal force to

accurately measure the lateral wheel-rail contact force. After compensation, it is found that the lateral contact force is almost constant with the different running speeds, as shown in Fig. 16d.

## 6. Measurement and control of contact forces in a 1/7 scaled V-Track

The discussion of the preceding sections is based on the configuration of V-Track shown in Fig. 1 (wheel diameter 200 mm and the standard rail profile S7), which is one of the different possible configurations of V-Track. In this section, the measurement and control of the wheel-rail contact forces are discussed with another configuration: the 1/7 scaled configuration, as shown in Fig. 17. In this configuration, the dimensions of the wheels and rails are 1/7 of the sizes of real-life wheels and rails. This is the maximum scale at which both the scaled wheels and the rails can be made from the corresponding real materials. The scaled wheels then have a diameter of 130 mm. In Fig. 17, the ring rail is 1/7 the size of UIC54E1, consisting of four sections of rails with different materials connected by rail joints. The parameters of the sleepers, fastenings and slab layer are chosen based on the similarity law [1,25] to make the track dynamic behaviors equivalent to those of the real systems. Only two wheel assemblies (W1, W3) equipped with the dynamometers were installed in V-Track.

In reality, the wheel-rail contact forces are influenced by many factors, such as axle loads, traction/braking, curve negotiation, and track and rail irregularities. The formation of rail defects is related to different wheel-rail contact conditions. For example, short pitch corrugation appears primarily in tangential tracks with relatively low axle loads and with no contact between the wheel flange and the rail gauge corner [26]. Head checks occur mainly on the outer rails of curves with radii of 500–3000 m, where a large lateral force arises at the rail gauge corner or shoulder [27,28]. Squats are usually caused by short-wavelength rail defects [29,30]. To simulate different wheel-rail contact conditions in real life, the control of wheel-rail contact forces in three directions is achieved in the 1/7 scaled V-Track, as shown in Fig. 18.

Fig. 18a shows that the longitudinal force is controlled by applying different braking torques from the braking motor. When the braking torque is zero, the torque on the wheel is negative and generates a braking force of approximately 200 N at the wheel-rail interface. The negative wheel torque arises from the resistance of the gearbox and the bearings of the braking motor. When the braking torque is  $-12$  N.m, the braking force increases to approximately 380 N. When the braking torque is 13 N.m, the negative wheel torque is compensated, and the longitudinal force slightly fluctuates around zero. Fig. 18b shows that the vertical force is controlled by wheel preloads, which are adjusted through the preload nuts. Different axle loads can thus be simulated in V-Track. The fluctuation of the vertical forces, which arises from vertical track irregularity, under different preloads has similar trends. Fig. 18c shows that the lateral force is controlled by adjusting the angle of attack. The impacts of the lateral forces at the four joints are much stronger than those of the longitudinal and vertical forces, which are probably caused by the sudden change of the angle of attack at the joints where fishplates were absent.



Fig. 17. The 1/7 configuration of V-Track.

Through effective control of wheel-rail contact forces, V-Track is expected to be capable of studying different types of defects in a real-life vehicle-track system. For instance, to study short pitch corrugation on straight tracks, the angle of attack should be set to approximately zero to minimize the influence of lateral contact force. However, to study squeal noise and corrugation in tight curves, we need to increase the angle of attack in order to reproduce the ‘stick-slip’ phenomenon [20].

## 7. Conclusions and future work

In this study, a force measurement system termed a dynamometer was developed to measure the wheel-rail contact forces in V-Track. The dynamometer consists of four 3-component piezoelectric force sensors and is mounted between the wheel assembly and the steel frame, which is in the load path from the wheel-rail interface to the frame on which V-Track is mounted. Static calibration of the dynamometer was first conducted, and high accuracy was achieved in measuring the static forces in three directions. Running tests were also carried out in V-Track.

The results showed that the designed dynamometer is capable of reliably and accurately measuring the wheel-rail contact forces. Utilizing the measurement results from the dynamometer, the control of these forces in the longitudinal, vertical and lateral directions was achieved by adjusting the braking torque, wheel preload and angle of attack, respectively.

In addition, the following observations were made.

- Compared to the longitudinal and vertical directions, the accuracy of the dynamometer in the lateral direction was lower, and the crosstalk errors from the other two directions were higher, probably because the lateral force was measured by compression of the piezo sensing elements instead of by shearing in the other two directions.
- Without braking torque from the braking motor, a negative torque due to resistance from the load path was measured on the wheel; this resistant torque generates a braking force at the wheel-rail interface. The torque can be compensated by applying an equal torque from the braking motor in the opposite direction.
- The offset of the wheel plane from the plane of guiding shafts was found to cause considerably large normal contact forces and friction forces between the guiding block and guiding shafts, which might potentially lead to relatively fast wear of the elements there, but it also enables the dynamometer to capture the high-frequency vibrations at the wheel-rail interface.
- Although the dynamometer can capture the dynamic features of the wheel-rail impact vibrations, a compensation method should be derived by considering the inertia of the wheel assembly to quantitatively measure the impact forces.

In summary, the wheel-rail contact forces of V-Track can be accurately measured and well controlled. In the future, we plan to use the 1/7 scaled V-Track to reproduce wheel and rail defects, such as rail corrugation, wheel polygonization, head checks and squats, to understand their formation mechanisms and develop the corresponding countermeasures. Further research on the compensation of the wheel inertia forces to more accurately measure the dynamic contact forces is also needed in future work. Since the dynamometer uses piezoelectric force sensors, signals inevitably drift over long-term measurement, which is a limitation of this system.

### CRedit authorship contribution statement

**Pan Zhang:** Conceptualization, Methodology, Software, Formal analysis, Data curation, Investigation, Writing - original draft, Writing - review & editing. **Jan Moraal:** Conceptualization, Methodology, Data curation, Validation, Investigation, Writing - review & editing. **Zili Li:** Conceptualization, Methodology, Resources, Writing - review & editing, Supervision, Project administration, Funding acquisition.

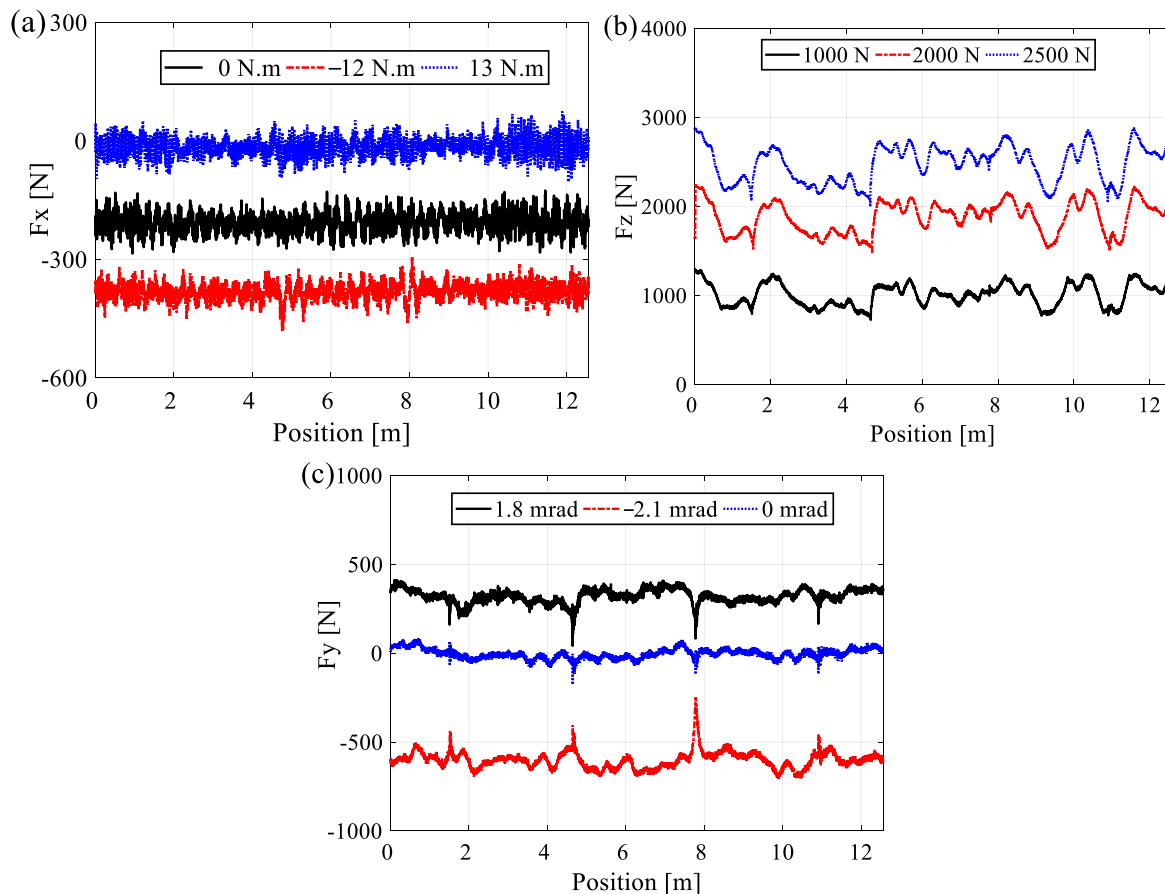


Fig. 18. Measurement and control of wheel-rail contact forces of W1 in the three directions. (a) Longitudinal force with different braking torques; (b) vertical force with different preloads; (c) lateral force with different angles of attack.

### Declaration of Competing Interest

The authors declare that they have no known competing financial interests or personal relationships that could have appeared to influence the work reported in this paper.

### Acknowledgements

This work was partly supported by the China Scholarship Council.

### References

- [1] M. Naeimi, Z. Li, R.H. Petrov, J. Sietsma, R. Dollevoet, Development of a New Downscale Setup for Wheel-Rail Contact Experiments under Impact Loading Conditions, *Exp. Tech.* 42 (1) (2017) 1–17, <https://doi.org/10.1007/s40799-017-0216-z>.
- [2] W.H. Zhang, J.Z. Chen, X.J. Wu, X.S. Jin, Wheel/rail adhesion and analysis by using full scale roller rig, *Wear* 253 (1–2) (Jul 2002) 82–88, [https://doi.org/10.1016/S0043-1648\(02\)00086-8](https://doi.org/10.1016/S0043-1648(02)00086-8).
- [3] A. Matsumoto, et al., Creep force characteristics between rail and wheel on scaled model, *Wear* 253 (1–2) (Jul 2002) 199–203, [https://doi.org/10.1016/S0043-1648\(02\)00100-X](https://doi.org/10.1016/S0043-1648(02)00100-X).
- [4] J. Brouzoulis, P.T. Torstensson, R. Stock, M. Ekh, Prediction of wear and plastic flow in rails-Test rig results, model calibration and numerical prediction, *Wear* 271 (1–2) (2011) 92–99, <https://doi.org/10.1016/j.wear.2010.10.021>.
- [5] J.R. Koch, N. Vincent, H. Chollet, O. Chiello, Curve squeal of urban rolling stock - Part 2: Parametric study on a 1/4 scale test rig, *J. Sound Vib.* 293 (3–5) (2006) 701–709, <https://doi.org/10.1016/j.jsv.2005.12.009>.
- [6] V. Garg, *Dynamics of railway vehicle systems*, Elsevier, 2012.
- [7] P. Gullers, L. Andersson, R. Lunden, High-frequency vertical wheel-rail contact forces - Field measurements and influence of track irregularities, *Wear* 265 (9–10) (2008) 1472–1478, <https://doi.org/10.1016/j.wear.2008.02.035>.
- [8] E. Gomez, J.G. Gimenez, A. Alonso, Method for the reduction of measurement errors associated to the wheel rotation in railway dynamometric wheelsets, *Mech. Syst. Sig. Process.* 25 (8) (2011) 3062–3077, <https://doi.org/10.1016/j.ymsp.2011.05.006>.
- [9] A. Matsumoto, et al., A new measuring method of wheel-rail contact forces and related considerations, *Wear* 265 (9–10) (2008) 1518–1525, <https://doi.org/10.1016/j.wear.2008.02.031>.
- [10] P. Urda, S. Munoz, J.F. Aceituno, J.L. Escalona, Wheel-rail contact force measurement using strain gauges and distance lasers on a scaled railway vehicle, *Mech. Syst. Signal Process.* 138 (2020). ARTN 106555 [10.1016/j.ymsp.2019.106555](https://doi.org/10.1016/j.ymsp.2019.106555).
- [11] A. Johansson, J.C.O. Nielsen, Out-of-round railway wheels—wheel-rail contact forces and track response derived from field tests and numerical simulations, *Proc. Inst. Mech. Eng., F: J. Rail Rapid Transit* 217 (2) (2006) 135–146, <https://doi.org/10.1243/095440903765762878>.
- [12] D. Milković, G. Simić, Z. Jakovljević, J. Tanasković, V. Lučanin, Wayside system for wheel–rail contact forces measurements, *Measurement* 46 (9) (2013) 3308–3318.
- [13] D. Cortis, M. Bruner, G. Malavasi, S. Rossi, M. Catena, M. Testa, Estimation of the wheel-rail lateral contact force through the analysis of the rail web bending strains, *Measurement* 99 (2017) 23–35.
- [14] K. Sekuta, P. Kolakowski, Piezo-based weigh-in-motion system for the railway transport, *Struct. Control Health Monitor.* 19 (2) (2012) 199–215.
- [15] F. Xia, C. Cole, P. Wolfs, An inverse railway wagon model and its applications, *Veh. Syst. Dyn.* 45 (6) (2007) 583–605.
- [16] F. Xia, C. Cole, P. Wolfs, Grey box-based inverse wagon model to predict wheel–rail contact forces from measured wagon body responses, *Veh. Syst. Dyn.* 46 (S1) (2008) 469–479.
- [17] L. Wei, J. Zeng, P. Wu, H. Gao, Indirect method for wheel–rail force measurement and derailment evaluation, *Veh. Syst. Dyn.* 52 (12) (2014) 1622–1641.
- [18] S. Meymand, M. Ahmadian, Design, development, and calibration of a force-moment measurement system for wheel–rail contact mechanics in roller rigs, *Measurement* 81 (2016) 113–122.
- [19] S. Yaldız, F. Ünsaçar, A dynamometer design for measurement the cutting forces on turning, *Measurement* 39 (1) (2006) 80–89.
- [20] Z. Yang, Z. Li, R. Dollevoet, Modelling of non-steady-state transition from single-point to two-point rolling contact, *Tribol. Int.* 101 (2016) 152–163.
- [21] Kistler, Instruction Manual: 3-Component Force Sensor Type 9067C, 9068C, 9066C4, Winterthur, Switzerland.
- [22] J. Kalker, Three-dimensional elastic bodies in rolling contact, 1990, *Solid Mech. Appl.* (1990).

- [23] Z. Yang, Z. Li, A numerical study on waves induced by wheel-rail contact, *Int. J. Mech. Sci.* 161–162 (2019), <https://doi.org/10.1016/j.ijmecsci.2019.105069>.
- [24] X. Zhao, Z. Li, The solution of frictional wheel–rail rolling contact with a 3D transient finite element model: Validation and error analysis, *Wear* 271 (1–2) (2011) 444–452, <https://doi.org/10.1016/j.wear.2010.10.007>.
- [25] A. Jaschinski, H. Chollet, S. Iwnicki, A. Wickens, J. Würzen, The application of roller rigs to railway vehicle dynamics, *Veh. Syst. Dyn.* 31 (5–6) (1999) 345–392.
- [26] S. Grassie, J. Kalousek, Rail corrugation: characteristics, causes and treatments, *Proc Inst. Mech. Eng., F: J. Rail Rapid Transit* 207 (1) (1993) 57–68.
- [27] R. Dollevoet, Z. Li, O. Arias-Cuevas, A method for the prediction of head checking initiation location and orientation under operational loading conditions, *Proc Inst. Mech. Eng., F: J. Rail Rapid Transit* 224 (5) (2010) 369–374.
- [28] A. Zoeteman, R. Dollevoet, Z. Li, Dutch research results on wheel/rail interface management: 2001–2013 and beyond, *Proc Inst. Mech. Eng., F: J. Rail Rapid Transit* 228 (6) (2014) 642–651.
- [29] Z. Li, X. Zhao, C. Esveld, R. Dollevoet, M. Molodova, An investigation into the causes of squats—correlation analysis and numerical modeling, *Wear* 265 (9–10) (2008) 1349–1355.
- [30] X. Deng, Z. Qian, Z. Li, R. Dollevoet, Investigation of the formation of corrugation-induced rail squats based on extensive field monitoring, *Int. J. Fatigue* 112 (2018) 94–105.